Ahmed, Hassan; Kuva, Jukka; Punkki, Jouni

Analysing entrapped pores in concrete via x-ray computed tomography : Influence of workability and compaction time

Published in:
Construction and Building Materials

DOI:
10.1016/j.conbuildmat.2024.135322

Published: 23/02/2024

Document Version
Publisher's PDF, also known as Version of record

Please cite the original version:
Ahmed, H., Kuva, J., & Punkki, J. (2024). Analysing entrapped pores in concrete via x-ray computed tomography : Influence of workability and compaction time. *Construction and Building Materials*, *417*, Article 135322.
https://doi.org/10.1016/j.conbuildmat.2024.135322

Construction and Building Materials 417 (2024) 135322

Contents lists available at ScienceDirect

Construction and Building Materials

journal homepage: www.elsevier.com/locate/conbuildmat

Analysing entrapped pores in concrete via x-ray computed tomography: Influence of workability and compaction time

Hassan Ahmed [a,*], Jukka Kuva [b], Jouni Punkki [a]

[a] Aalto University, Department of Civil Engineering, Espoo 02150, Finland
[b] Circular Economy Solutions, Geological Survey of Finland, 02150 Espoo, Finland

A R T I C L E I N F O

Keywords:
Entrapped pores
Concrete compaction
Concrete workability
Concrete porosity
X-ray computed tomography

A B S T R A C T

Understanding the attributes of entrapped pores in compacted concrete is crucial for improving mechanical and durability properties of concretes. This research investigates how compaction time and workability affect entrapped pores characteristics. Using X-ray Computed Tomography, concrete specimens, with different workability classes, were analysed after being compacted for different times. Results show that increased workability and vibration time significantly reduce entrapped porosity, especially in the 2.7–4.6 mm diameter range, but this effect lessens at extended durations. Higher workability results in less spherical pores, potentially leading to stress concentrations. Additionally, concentrations of entrapped pores up to 5% were observed along specimen heights. These insights contribute to our understanding of pore properties, indicating potential adverse impacts on the performance of concrete.

1. Introduction

Concrete is an inherently porous material, a characteristic that significantly influences its durability and mechanical properties [1–8]. According to Mehta and Monteiro [5], pores in concrete can be categorized into four groups based on their size: gel pores, capillary pores, entrained pores, and entrapped pores, each differently impacting the properties of concrete.

Gel pores, ranging from 0.5 to 2.5 nm, constitute the interparticle spaces between calcium silicate hydrates, influencing drying shrinkage and creep. Capillary pores, with sizes between 0.01 μm and 5 μm, impact the permeability of concrete. Entrained pores, which range from 50 μm to 1 mm, are deliberately introduced via air-entraining chemical admixtures to enhance freeze-thaw durability [1,2,6]. Entrapped pores, representing 5% to 20% of the fresh concrete volume [9], are larger than 1 mm and are introduced into the concrete during mixing and placement [5].

It should be noted that the threshold for defining entrapped pores differs across standards. For instance, ASTM C457 [10] acknowledges that distinguishing between entrapped and entrained air voids is challenging due to the overlapping characteristics of these voids. Hence, it does not provide a precise limit, stating that such a distinction can be somewhat arbitrary. On the other hand, the Finnish standard for concrete quality control [11] is more specific, setting the threshold for entrapped pores at 0.8 mm.

Ideally, entrapped pores should be removed through compaction [9,12], as they can reduce strength [1,9] and density [9] of concrete, as well as adversely affect its durability [5,9]. Moreover, entrapped air contributes to poor bonding of concrete with reinforcement [9]. Neville [13] reported that concrete compressive strength may decrease by approximately 5% for every 1% increment in air content, i.e., entrapped, and entrained air combined. In a separate study, Chung et al. [1] observed a more variable relationship, with strength reductions between 5% and 9% per 1% air content increase.

Since the mix design deliberately includes air-entrainment [1,2,6], the risk of strength decrease [1,9] is predominantly attributed to unwanted entrapped pores that remain in concrete due to poor compaction. Hence, the removal of entrapped air through compaction is an essential process for achieving stronger and more durable concrete. On the other hand, excessive compaction of concrete can lead to segregation, a phenomenon where heavier aggregates sink towards the bottom and lighter ones rise upwards within the paste matrix [9,12]. This causes further durability problems and uneven density distribution in the concrete [14]. Therefore, it is crucial to assess the presence of compaction pores in concrete to evaluate its durability and strength, while considering the potential issue of segregation.

* Correspondence to: Department of Civil Engineering, School of Engineering, Aalto University, Rakentajanaukio 4, Room 221, 02150 Espoo, Uusimaa, Finland.
E-mail address: hassan.ahmed@aalto.fi (H. Ahmed).

https://doi.org/10.1016/j.conbuildmat.2024.135322
Received 5 July 2023; Received in revised form 31 January 2024; Accepted 2 February 2024
Available online 10 February 2024

A variety of methods are available for assessing air content of concrete and its pore structure. One of the standardized methods to determine the total air content is the pressure method [15], which involves applying a known pressure to a specific volume of concrete within a chamber and measuring the resulting volume change. However, it is important to note that this method assumes perfect compaction and attributes the observed volume change solely to entrained air, potentially overlooking the influence of entrapped pores on the results. Manual measurements [16] can be employed to determine entrained air void properties in hardened concrete, involving the examination of polished samples under a microscope. This process demands significant skill, time, and expertise. Although automated techniques like digital image processing [1,7,17,18] are gaining popularity for their objectivity, these methods are still time-consuming in terms of sample preparation, and they primarily focus on 2D pore analysis while concrete pores exist in a 3D distribution.

To overcome the limitations of digital image processing, researchers have used x-ray computed tomography (XCT) to analyse the properties of entrained air voids in hardened concrete [1–3,7,19–27]. A standard laboratory XCT system comprises an x-ray source, a sample on a rotation stage, and a planar detector. Minimal sample preparation is typically needed, and the achievable resolution is mostly determined by the sample size. During CT scanning, multiple 2D projection images are obtained as the sample rotates, which are used to create a 3D volumetric dataset.

The reconstructed dataset contains a 3D arrangement of volumetric pixels (voxels) with brightness levels corresponding to the x-ray density of the material, which is associated with both physical density and atomic mass [3]. This dataset is displayed in a matrix where each row contains the X, Y, Z coordinates of a voxel's centre and its associated grayscale value. Within this framework, pores are represented by the lowest greyscale values. During post-processing, pore voxels can be segmented using various methods, such as watershed segmentation [28], based on their greyscale values.

In the scope of porosity investigations, XCT has been employed not only to analyse the total air content of concrete [1,2,7,8,20–22,25,26], but also its pore size distribution [1,2,7,8,25,27]. These properties encompass both entrained and entrapped air. In studies [8] and [26], the sample volumes were as large as 196 cm^3 and 126 cm^3 , respectively, to improve the sample representability of the total air content values. Furthermore, researchers have investigated specific properties of entrained air pores such as, spacing factor [20–22], paste-void spacing [21,23], pore orientation [25], sphericity of the pores [2,25], and specific surface of air-void system [21]. Assessment of freeze-thaw durability and permeability of concrete were among the main purposes behind studying the previously mentioned properties. However, when studying properties such as spacing factor and specific surface of the air-void system for entrained pores [21,23–25], the samples must be sufficiently small, which can obstruct precise assessment of the total air content [21]. In applications specifically focusing on these properties, the volume of the scanned samples ranged from 1 cm^3 to 64 cm^3 only, with scanning resolutions from 6.2 μm to 30 μm.

Most of the research mentioned above focuses on the study of entrained pores in concrete. The limited attention given to entrapped air is due to the assumption that concrete is compacted until entrapped pores are minimized, achieving the desired density and strength [9]. However, completely eliminating entrapped pores is impractical [9]. Popovics [29] and Neville [13] mentioned that approximately 1% of entrapped air remains in concrete even after proper compaction. Mehta and Monteiro [5] stated that the amount of entrapped air left in non-air-entrained concrete after compaction can range from 0.2% to 3% for maximum aggregate sizes values from 9.5 mm to 150 mm, respectively. In the case of air-entrained concrete, no specific limits for entrapped air percentages were provided; instead, the total air content was specified. Furthermore, while both the European standard EN 206:2014 [27] and the ACI report 309R-05 [9] emphasize the importance of minimizing entrapped pores in concrete after compaction, they do not specify a threshold for acceptable levels of entrapped air.

This research primarily aims to investigate the presence of potentially excessive entrapped pores in hardened concrete cores using XCT. To achieve this, we conducted an experiment where concretes with different consistencies were compacted with a vibration table for similar durations. Subsequently, cores were drilled from these samples and subjected to XCT scanning to gather data about the presence and characteristics of entrapped pores. The acquired pore data was quantitatively analysed to extract information regarding the amount, location, and shape of the entrapped pores within each concrete sample, and comparisons were made across all samples. Additionally, the segregation levels of the concrete samples were investigated through density measurements at various depths.

2. Materials and methods

2.1. Materials and mix composition

The concrete mixes were proportioned using OIVA cement CEM II/B-M (S-LL) 42.5 N, produced by Finnsementti (Parainen, Finland), which has a specific gravity of 3.15. OIVA cement has 21–35% added limestone and ground granulated blast-furnace slag, and its chemical composition is shown in Table 1.

The aggregate used in this study was granitic gravel with a specific gravity of 2.68. For all mixes, a combination of seven aggregate fractions was used, with the largest aggregate size being 16 mm. Table 2 presents the size distribution and proportion of each aggregate fraction in the mix. The concrete mixes comprised 425 kg/m^3 of cement, 170 kg/m^3 of effective water, and 1709 kg/m^3 of aggregates. The water absorption for all the aggregate fractions was 0.8%, resulting in an effective w/c ratio of 0.40.

In addition, three different dosages of superplasticizer and air-entraining agent were used to formulate three mixes each with a different consistency but similar air content. The air-entraining agent, MastersBuilders MasterAir 100 (Riihimäki, Finland), and the superplasticizer, MasterBuilders MasterGlenium SKY 600 (Riihimäki, Finland), were used for this purpose. The target slump classes were S2, S3, and S4, with superplasticizer dosages of 0.35%, 0.56%, and 0.71% by cement weight, respectively. To keep the air entrainment level constant at 5%, the air-entraining agent dosages were adjusted to 0.008%, 0.011%, and 0.020% of the cement weight for the S2, S3, and S4 concretes, respectively. All materials were stored and utilized at a stable room temperature (20 ± 2 °C).

2.2. Concrete casting, standard tests, and compaction

A pan-type mixer was used to prepare 40-liter batches of concrete for each slump, i.e., three different castings. Two fresh concrete tests were performed after mixing: the slump test [30] and the air content test via pressure method [15]. In cases where the mixture failed to achieve the previously mentioned target slump and/or air content, it was discarded, and a fresh batch of concrete was prepared until the targeted properties were obtained.

For each slump class, three cylindrical steel moulds, with diameter of

Table 1
The chemical composition of OIVA cement CEM II/B-M (S-LL) 42.5 N.

Chemical composition	Mass percentage volume (%)
CaO	63–65
SiO_2	20–22
Al_2O_3	4.0–5.4
Fe_2O_3	2.8–3.3
MgO	2.5–3.2
SO3	3.0–3.3

Table 2
Combined aggregate size composition and distribution of the mixture.

Aggregate type	Fraction (Diameter in mm)	Portion (%)	Sieve size (mm)									
			0.125	0.25	0.5	1.0	2.0	4.0	8.0	16.0	32.0	64.0
Filler	Filler 96	7	42	81	93	97	98	100	100	100	100	100
Fine Aggregates (FA)	0.1 – 0.6	10	3	21	76	100	100	100	100	100	100	100
	0.5 – 1.2	13	0	2	6	70	100	100	100	100	100	100
	1.0 – 2.0	13	0	1	2	7	79	100	100	100	100	100
	2.0 – 5.0	16	0	0	1	1	1	47	100	100	100	100
Coarse Aggregates (CA)	5.0 – 10.0	18	0	0	0	0	0	3	82	100	100	100
	8.0 – 16.0	23	0	0	0	0	0	0	5	99	100	100
	Total (%)	100										
	Combined Aggregates (%)		3	8	15	27	40	51	75	100	100	100

150 mm and height of 300 mm, were filled with concrete, yielding a total of nine specimens for the entire experiment. The moulds were filled in one layer, and the concrete placement was kept as constant as possible to avoid varying entrapment of air. Afterwards, compaction was performed using a compaction table with a fixed vibration frequency of 50 Hz, and a stopwatch was used to record the compaction duration. Each slump class had three different vibration times: 5 s, 20 s, and 45 s, with the intent of leaving high, medium, and low amounts of entrapped pores in the specimens, respectively.

After compaction, the specimens were covered and left to harden for 24 h before demoulding. The specimens were named using a combination of slump class and vibration time. The naming convention starts with the slump class followed by a dash, and then the vibration time. For example, S2–5 represents a specimen with a slump class of S2 and a vibration time of 5 s, while S4–45 is a specimen with an S4 slump class that was vibrated for 45 s, and so on. The compaction times were selected to represent durations that are shorter than optimal (5 s), within the normal range (20 s), and longer than necessary (45 s) for achieving proper compaction.

2.3. X-ray Computed Tomography (XCT)

A core measuring 70 mm in diameter was drilled from the centre of each specimen, matching the height of the respective specimen as shown in Fig. 1. The core dimensions were selected to ensure adequate x-ray penetration, while simultaneously capturing a substantial portion of the original specimen. Specifically, each core's volume of 1155 cm^3 constitutes around 23% of the total specimen volume.

Fig. 1. The nine hardened concrete specimens with 70-mm cores drilled centrally.

The samples were scanned using the 240 kV microfocus tube with 0.5 mm of copper and 0.5 mm of aluminium as beam filters. Accelerating voltage was 180 kV and tube current 350 μA for a total power of 63 W. At each angle, the detector waited for a single exposure time of 500 ms and then took an average over three exposures of 500 ms. The image resolution was 50.0 μm. Samples were imaged as a multiscan, where several fields of view displaced vertically from each other were connected to a single 3D file, with 2000–2500 angles at each field of view, depending on the sample. All scans consisted of five fields of view for a total scan time of 5.55–6.95 h. No ring artifact reduction was used for any of the samples in reconstruction, and the beam hardening correction coefficient (0−10) was 4. Data was then reconstructed using the phoenix datos|x 2 reconstruction software and analysed using ThermoFisher PerGeos 2020.2. The sample surface was determined using the Mask segmentation recipe and the pores were segmented using the 2-Phase Watershed recipe.

2.4. Density measurements

Evaluating the density variation within concrete specimens is crucial for determining the segregation level. Therefore, after XCT scanning of the cores, they were sliced into 10 discs with a thickness of around 25 mm using a diamond blade saw. The discs were numbered from 1 to 10, with disc 1 at the top and disc 10 at the bottom. The density of each disc was subsequently measured following the European standard EN 12390–7 [31]. This method made it possible to create density profiles for each specimen, illustrating how density fluctuates in relation to the height of the concrete.

3. Results and discussion

3.1. Workability and air content

The results of the fresh concrete tests for each casting are shown in Table 3. Castings #1, #2, and #3 satisfied the target slump classes of S2, S3, and S4, respectively. The target air content for this research was set to 5.0%. However, due to inherent variations in concrete mixing and testing, the achieved air content varied slightly, with values of 5.1%, 5.6%, and 5.4% for the respective slump classes of S2, S3, and S4. This slight deviation from the target is expected and does not significantly impact the behaviour of concrete during compaction or the characteristics of the final hardened concrete. Especially as the focus of this study is on entrapped pores, these minor air content variations are not expected to affect the subsequent analyses and findings.

Table 3
Slump and air content values for the three castings.

Casting	Slump (mm)	Slump class	Air content
No. 1	70	S2	5.1%
No. 2	110	S3	5.6%
No. 3	189	S4	5.4%

3.2. XCT analysis

In the following sections of "XCT analysis", the results pertaining to entrapped pores in the concrete specimens will be presented and discussed. First, the total volume of entrapped pores, i.e., entrapped porosity, across different slumps and vibration times will be examined. This will be followed by an investigation into the dispersion of these pores along the height of the cores. Subsequently, the pore size distribution within each specimen will be analysed, and finally, the sphericity of the pores will be evaluated.

3.2.1. Total entrapped pores

Table 4 illustrates the total volume of entrapped pores within each core. While Popovics [29] suggested that approximately 1% of entrapped pores typically remain in concrete after compaction, this research follows the more commonly accepted practice in the Finnish concrete industry, which allows for up to 2%. As shown in Table 4, across all cores, the entrapped porosity remained under the 2% limit, apart from core S2–5, which exhibited a higher entrapped porosity of 2.2%.

Fig. 2 displays a representation of 3D reconstructed entrapped pores in concrete specimens S2–5, S2–20, and S2–45, showcasing the impact of different compaction times. Specimen S2–5 (Fig. 2a) exhibits a high density of entrapped pores of varying sizes, distributed throughout the entire height of the specimen. A pronounced change is observed in specimen S2–20 (Fig. 2b), where there is a notable reduction in the overall concentration of pores. Most of the remaining larger pores in S2–20 are located closer to the upper region of the specimen. In comparison, specimen S2–45 (Fig. 2c) shows a further decrease in the number of entrapped pores, especially those of larger sizes. This progression across the specimens underscores the influence of compaction time in reducing entrapped porosity. The entrapped porosity profiles and actual pore size distribution for the 9 studied specimens is explained in detail in subchapters 3.2.2 and 3.2.3, respectively.

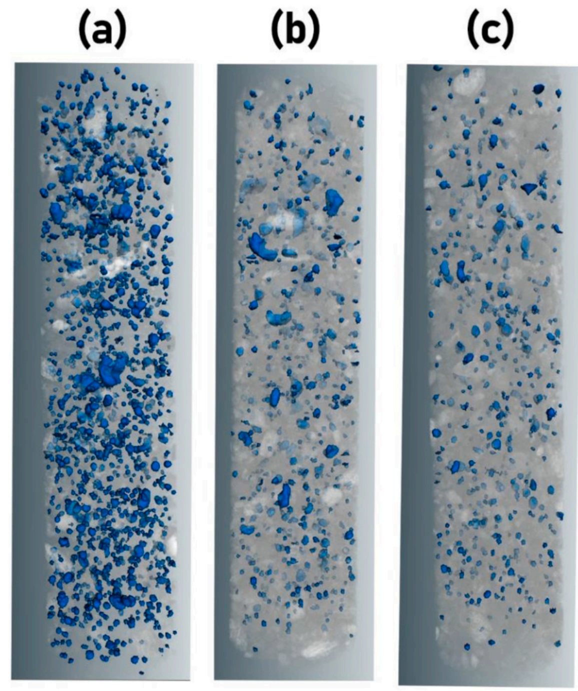

Fig. 2. Two-dimensional representation of 3D reconstructed entrapped pores in specimens: (a) S2–5, (b) S2–20, (c) S2–45.

Fig. 3 illustrates the relationship between entrapped porosity and vibration time for the different slumps. As expected, an increase in vibration time leads to a reduction in entrapped air within the concrete. For each vibration time group, the average entrapped porosity is approximately 1.8% for 5 s, 1.3% for 20 s, and 0.7% for 45 s. Notably, extending vibration time from 20 to 45 s yields a significant drop in entrapped porosity, with reductions of about 50%, 30%, and 40% for slumps S2, S3, and S4 respectively. However, this decrease should be considered alongside potential issues such as segregation, a topic further explored in subchapter 3.3.

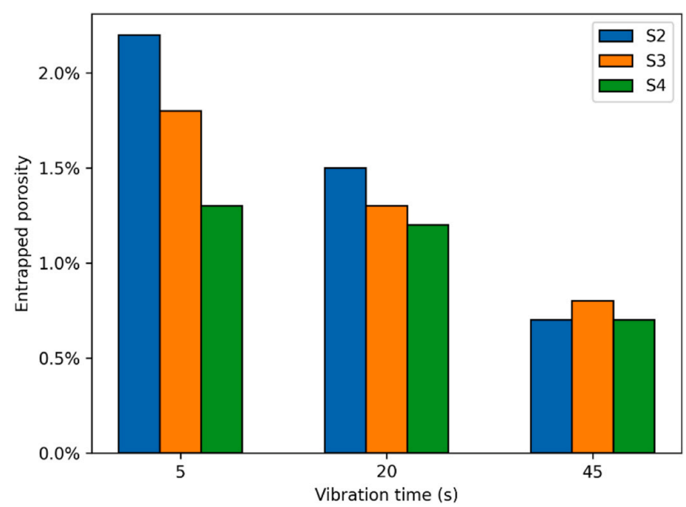

Fig. 3. A column chart of the entrapped porosities for the different slump classes and compaction times.

Furthermore, within each time group, the consistency of the concrete also affected the entrapped porosity. Stiffer concretes, represented by the S2 slump group, exhibit higher entrapped porosity for equivalent vibration times. For example, S2–5 holds 0.7%-unit more entrapped air than S3–5, which in turn contains 0.5%-unit more entrapped air than S4–5. A similar pattern was observed in the 20-second group, with S2–20 showing 0.2%-unit more entrapped porosity than S3–20%, and 0.3%-unit more entrapped air than S4–20. However, this trend diminishes for the 45-second group, where S2–45 and S4–45 have the same entrapped porosity, and S3–45 contains 0.1%-unit more. This can be attributed to the low entrapped porosity values at this vibration duration, all under 1%, suggesting that the maximum amount of entrapped air had been expelled, leading to only minor differences between specimens.

3.2.2. Entrapped porosity profiles

Fig. 4 presents the profiles of entrapped porosity, obtained by calculating the volume average of entrapped pores in each 0.1-mm slice of the cores. Each core was analysed in approximately 2850 such slices. The entrapped porosity profiles for the S2-group are presented in the top row of Fig. 4. While the 2% limit is commonly employed to evaluate the total entrapped porosity, in this research, we have adopted it as a reference point to assess the maximum entrapped porosity within a core. This choice stems from the absence of a more specific limit for the local maximum entrapped porosity in existing guidelines or standards.

In the S2–5 sample, the 2% threshold is frequently surpassed

Table 4
Total amount of entrapped pores in each sample obtained via x-ray computed tomography.

Sample	S2-5	S2-20	S2-45	S3-5	S3-20	S3-45	S4-5	S4-20	S4-45
Entrapped porosity	2.2%	1.5%	0.7%	1.8%	1.3%	0.8%	1.3%	1.2%	0.7%

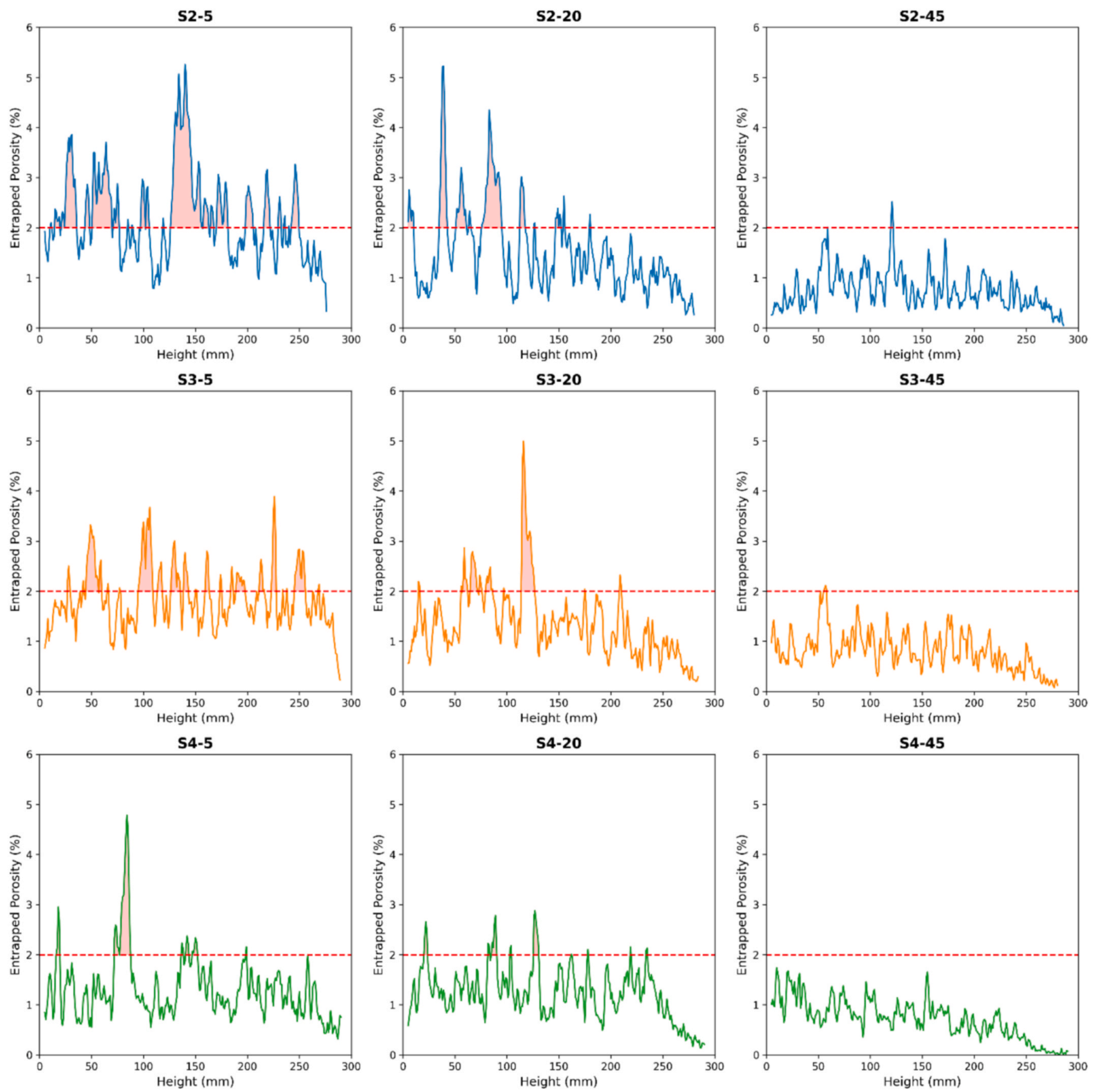

Fig. 4. Entrained porosity profiles for the nine concrete specimens. The top row corresponds to S2 concrete samples, the middle row to S3 samples, and the bottom row to S4 samples. The red dashed line represents the 2% porosity threshold commonly accepted in the Finnish concrete industry.

throughout the core, indicating a wider distribution of high porosity regions. The S2–20 sample presents fewer heights where the 2% threshold is exceeded, suggesting a less uniform distribution of high porosity regions due to a longer compaction time. Lastly, the S2–45 sample demonstrates a concentrated distribution of entrapped porosity, with only a minor spike above the 2% threshold. This trend implies that extended compaction time leads to a more contained distribution of high porosity areas within the concrete.

A similar trend is displayed in the S3 and S4 samples shown in the second and third rows of Fig. 4, respectively. S3–5 exceeds the 2% limit frequently throughout the height of the core, whereas S3–20 exceeds the limit much less, and finally S3–45 barely crosses over that limit. Similarly, S4–5 surpasses the 2% threshold at more heights than S4–20, whereas S4–45 remains below that limit for the whole height of the core. These observations confirm that longer compaction times lead to more contained entrapped porosity profiles across all groups (S2, S3, and S4), supporting the conclusion that extended compaction effectively minimizes the instances of high porosity within concrete samples.

In addition to examining the effect of compaction time, the influence of concrete slump can be checked by considering the vertical columns in Fig. 3. The area under the porosity curves that exceeds the 2% threshold (highlighted in red) notably decreases as the slump increases, particularly for samples compacted for 5 and 20 s. This observation suggests that for concretes with higher workability, porosity profiles stay more consistently below the 2% threshold given the same vibration time. Conversely, both S2–45 and S3–45 samples display a minimal fraction of porosity exceeding this threshold, whereas S4–45 consistently remains beneath it. These trends can be attributed to the extended vibration time, which significantly reduces entrapped air in the specimens, approaching the maximum possible removal, thereby reducing variations across different slump values.

A quantitative analysis was carried out to assess the regions where porosity surpasses the 2% threshold, i.e., high-porosity regions. This process involved determining the height fractions in each sample with porosity surpassing this benchmark. These fractions were estimated using the trapezoidal rule to calculate the area under the curve of each porosity profile – the areas highlighted in red in Fig. 3. The outcomes of this analysis are presented in Table 5.

For the S2-group, the percentage of sample height at high-porosity regions decreases by over 60% from 66% for S2–5 to 4% in S2–45. Similarly, an over 40% decrease is observed when the vibration time is increased from 5 s to 20 s for the S3-group, and a 22% decrease is seen within the S4-group. Similarly, when examining the impact of increasing the workability of concrete on the occurrence of high-porosity regions, it is observed that with a vibration time of 5 s, there is a 20% decrease in the percentage from S2 to S3, followed by a further 24% decrease from S3 to S4. Likewise, for 20 s of vibration, the area decreases by 13% from S2 to S3, and by 6% from S3 to S4. Finally, the specimens vibrated for 45 s show little variation among each other, with S2–45 and S3–45 having only 4% of their height with entrapped porosity over 2%, and S4–45 having none.

Furthermore, Table 5 provides the maximum entrapped porosity observed in each sample and its location. It is evident that the maximum entrapped porosity exceeds the 2% threshold for all specimens except for S4–45. Notably, in samples such as S2–5, S2–20, S3–20, and S4–5, the maximum entrapped porosity surpasses the 2% threshold by nearly double, which raises concerns about the potential formation of weaker spots at those specific locations.

A general trend of decreasing maximum entrapped porosity is observed as we progress from the S2 to S4 groups and within the S2 and S4 groups from a compaction time of 5 s to 45 s. This observation resonates with our earlier discussions that extended compaction time and increased workability effectively reduce the overall entrapped porosity within the concrete samples. An exception to this is the S3 group, where 5 s of vibration left a maximum entrapped porosity of 3.9%, whereas 5.0% entrapped porosity remained after compacting for 20 s. This discrepancy observed in the S3 group may be caused by minor variations in the placement process or in the distribution of aggregates within the specimens, both of which could influence the formation and migration of entrapped pores. It is also worth noting that S2–5 and S2–20 show almost the same maximum entrapped porosity of 5.3% and 5.2% respectively, which can be explained by the low workability making it harder for entrapped air to escape, when compared to the more flowable concretes of the S3 and S4 groups, where the maximum entrapped porosity values are consistently lower as the compaction time increases.

Based on the previous observations, it can be deduced that although the total entrapped porosity (see Section 3.2.1) and the percentage of height with porosity > 2% both drop as the compaction time increases for the different slump groups, the maximum entrapped porosity does not necessarily follow a similar trend, as is the case between S2–5 and S2–20, which both have almost the same maximum entrapped porosity, or S3–20 that has 1.1%-point higher maximum entrapped porosity than its less compacted counterpart S3–5.

Assessing the locations of maximum porosity in the samples, we see considerable variability. Typically, high-porosity regions are in the first half of the sample, aligning with the upward migration of entrapped pores during compaction. However, as indicated in Table 5, the exact location of maximum entrapped porosity varies significantly, from as close as 10 mm to as far as 226 mm from the top of the specimens, as observed in S4–45 and S3–5 respectively. This variance further highlights the complexity of the expulsion process of entrapped pores through compaction.

In summary, the presence and concentration of high-porosity ranges in the samples reveal important insights into the behaviour of air entrapment during compaction. Notably, these findings highlight the occurrence of localized areas within the concrete with high levels of entrapped air, reaching up to 5%. This aspect of air distribution has not been extensively explored in previous studies, emphasizing the need for further investigation into its impact on the durability and strength of concrete.

3.2.3. Pore size distribution

To analyse the distribution of entrapped porosity in each sample, several key summary statistics were calculated using data from our XCT analysis. Firstly, the equivalent diameter of each pore was determined, representing the diameter of a sphere with the same volume as the pore. Secondly, we calculated the minimum, maximum, mean, and the three quartiles (the 25th, 50th, and 75th percentiles) for the equivalent diameters of entrapped pores. The focus was on entrapped pores with a minimum diameter of 0.8 mm, corresponding to an equivalent volume of approximately $0.268\ mm^3$. The results of these calculations are presented in Table 6.

It is evident that there is a significant degree of variability in the maximum equivalent diameter across the samples, with diameters ranging from 6.4 mm up to 12.4 mm. This disparity becomes even more pronounced when compared to the minimum equivalent diameters, where the maximum values are found to be disproportionately larger. Specifically, the maximum equivalent diameters are almost 8 to 15 times

Table 5
Characteristic of high-porosity regions (regions above the 2% entrapped porosity threshold).

Sample	Percentage of Sample Height with Entrapped Porosity > 2%	Max Entrapped Porosity	Max Entrapped Porosity Location from Top
S2-5	66%	5.3%	140 mm
S2-20	41%	5.2%	39 mm
S2-45	4%	2.5%	121 mm
S3-5	46%	3.9%	226 mm
S3-20	28%	5.0%	116 mm
S3-45	4%	2.1%	57 mm
S4-5	22%	4.8%	84 mm
S4-20	14%	2.9%	127 mm
S4-45	0%	1.7%	10 mm

Table 6
Summary statistics for equivalent diameters of entrapped pores. Q1, Q2, and Q3 represent the 25th, 50th, and 75th percentiles.

Specimen	S2-5	S2-20	S2-45	S3-5	S3-20	S3-45	S4-5	S4-20	S4-45
Minimum equiv. diameter (mm)	0.8	0.8	0.8	0.8	0.8	0.8	0.8	0.8	0.8
Maximum equiv. diameter (mm)	12.4	12.3	6.4	8.6	11.6	8.4	9.5	8.7	6.8
Mean equiv. diameter (mm)	1.7	1.7	1.5	1.6	1.7	1.5	1.5	1.6	1.5
Q1 equiv. diameter (mm)	0.9	0.9	0.9	0.9	0.9	0.9	0.9	0.9	0.9
Q2 equiv. diameter (mm)	1.05	1.0	1.0	1.0	1.0	1.0	1.0	1.0	1.0
Q3 equiv. diameter (mm)	1.4	1.4	1.3	1.4	1.4	1.3	1.3	1.3	1.3

greater than the minimum equivalent diameters. This high discrepancy highlights the broad range of diameters within the samples.

Additionally, the data exhibits a notable right skew, as evidenced by the mean equivalent diameter being, on average, 1.5 times larger than the median (second quartile). Further supporting this observation are the relatively close quartile values. There is an average difference of just 0.1 mm between the first and second quartiles, and 0.3 mm between the second and third quartiles. These values are considerably smaller than even the smallest maximum volume, with an average discrepancy of over 8 mm. These statistical observations demonstrate the presence of a large quantity of small pores and a disproportionately smaller number of larger ones within each concrete sample.

Fig. 5 provides further evidence by displaying the relative frequencies of pores across various volume ranges. About 70% of pores in all samples fall within a volume range of 0.27–1 mm^3 (equivalent diameter range of 0.8–1.2 mm). The next most frequent volume range, 1–2 mm^3 (equivalent diameter range of 1.2–1.6 mm), accounts for approximately 15% of the pores.

In the previous analysis, the relative frequency of pores within defined volume ranges was explored. Pivoting to a more volumetric approach, we evaluated the respective contributions of each volume range to the total entrapped porosity in the samples. As shown in Fig. 6, the volume range 10–50 mm^3 (equivalent diameter range of 2.7–4.6 mm) demonstrates the highest contribution to the total entrapped porosity, exhibiting an average volumetric fraction of 25% across the samples combined. The reasons behind this significant contribution of the volume range 10–50 mm^3 are not fully clear, but factors such as vibration frequency or aggregate gradation may play a role, requiring further investigation. Although, for all specimens, around 70% of the pores were within the volume range 0.27–1 mm^3 (see Fig. 5), this volume range represents on average 17% only of the entrapped porosity (see Fig. 6).

The distribution of total entrapped porosity among different volume ranges is generally consistent across most specimens, regardless of slump or vibration time. However, two notable exceptions emerge from the analysis. Firstly, in the case of S2–20, the volume range of 100–500 mm^3 contributes significantly higher, representing 23% of the entrapped porosity, whereas for S2–45, it constitutes only 4%. On average, the remaining seven specimens exhibit a 9% contribution from this volume range.

Secondly, the presence of pores within the 500–1000 mm^3 range is exclusive to specimens S2–5, S2–20, and S3–20, constituting 4%, 11%, and 11% of the total entrapped porosity, respectively. Although it was expected that S3–5 would contain a higher proportion of larger pores compared to S3–20, which was vibrated for 15 s longer, the analysis revealed the opposite. S3–20 exhibits 11% of the entrapped porosity within the volume range of 500–1000 mm^3 , while S3–5 has no contribution in that range. This discrepancy highlights the lack of a consistent pattern in the distribution of entrapped pores at higher diameter ranges (>9.8 mm).

3.2.4. Sphericity of entrapped pores

We calculated the true sphericity index, as defined by Wadell (1932) and cited in [32], to estimate the sphericity of each entrapped pore within the samples. The equation for the sphericity index is given by:

$$\psi = \frac{\sqrt[3]{36\pi V^2}}{S} \quad (1)$$

where ψ is the sphericity index, V represents the volume of the pore, and S denotes the surface area of that pore. The true sphericity index ranges from 0 to 1, with 1 being a perfect sphere. The computed sphericity indices were used to create a cumulative distribution plot, with sphericity indices on the x-axis and the corresponding cumulative distributions of pores on the y-axis, as shown in Fig. 7.

Turning our focus to the S2-group first, Fig. 7 reveals a sphericity index that predominantly surpasses 0.5. In fact, across all three samples (S2–5, S2–20, and S2–45), only an average of 1% of pores exhibit a sphericity index of 0.5. Additionally, almost half of the pores are close to perfect spheres with sphericity indices of 0.8 and 0.9. For instance, the percentage of pores that have a sphericity index of 0.9 for S2–5, S2–20, and S4–45 is 59%, 47%, and 26% respectively.

On the other hand, for the S3-group, around 9% of entrapped pores have a sphericity index of 0.5, which is 8%-point higher than that in S2-group. In addition, the overall sphericity decreases compared to the S2-group, as S3–5, S3–20, and S3–45 have 41%, 15%, and 7% of their pores with a sphericity index of 0.9, respectively. A similar drop is observed as we increase the slump further to S4, as for the S4-group around 22% of the pores have a sphericity index of 0.5. Moreover, S4–5, S4–20, and S4–45 have only 11%, 3%, and 2% respectively of their pores with a sphericity index of 0.9.

Our observations indicate a trend where an increase in concrete workability correlates with a decrease in the sphericity of its entrapped

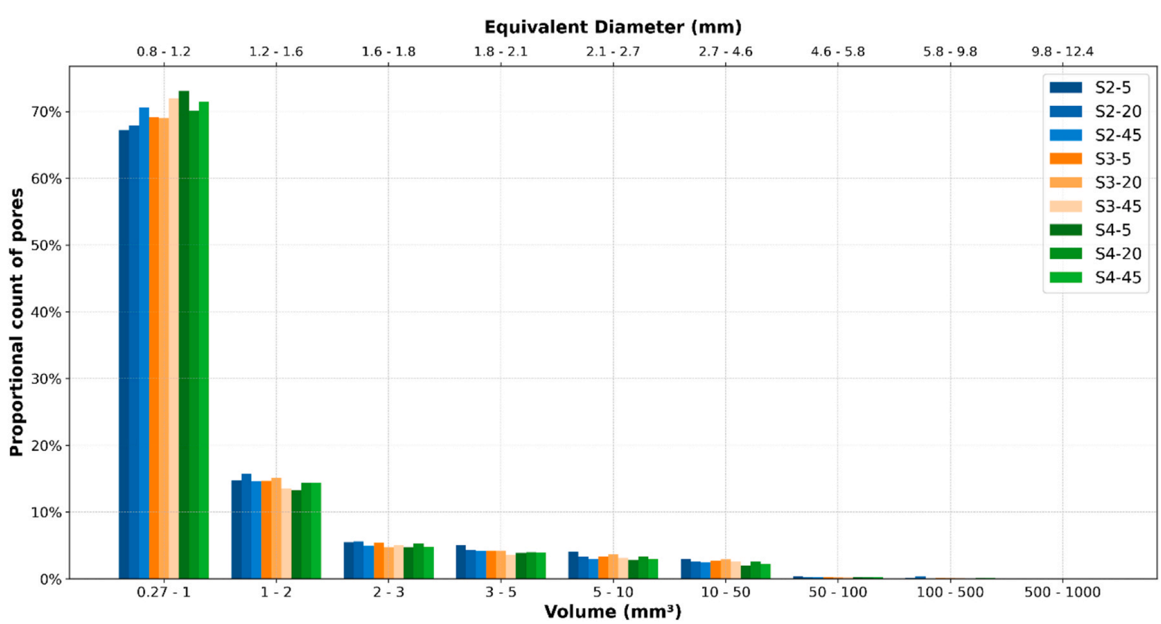

Fig. 5. The proportional count of pores within each predefined volume range and their equivalent diameter ranges.

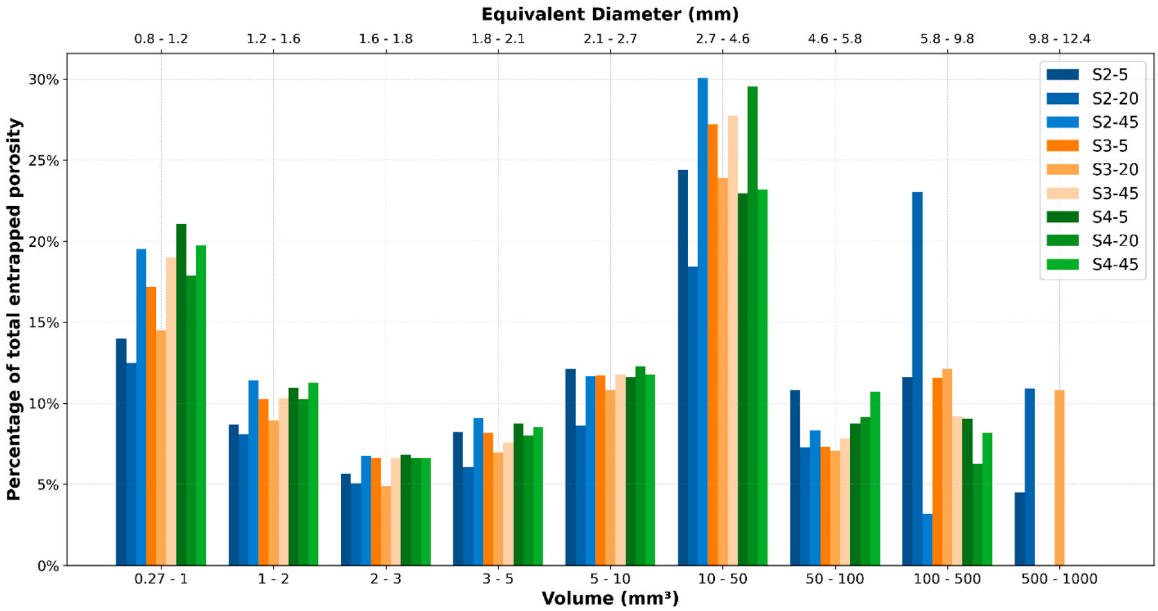

Fig. 6. The relative contribution of pore volumes within each predefined volume range (and their equivalent diameters) to the total entrapped porosity.

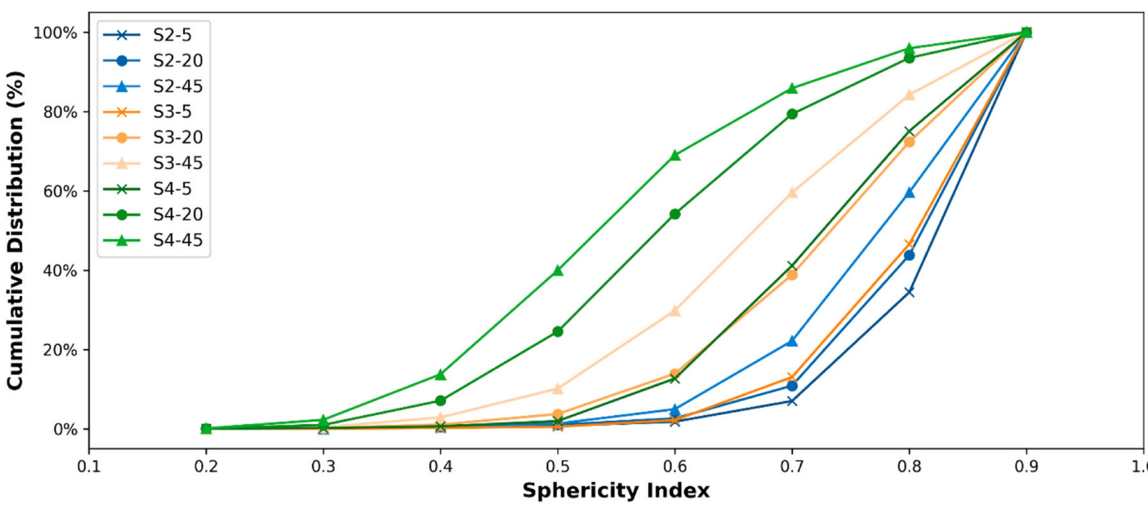

Fig. 7. Cumulative distribution curves of pore sphericity indices for the nine different concrete specimens.

pores. This trend might be explained by two main factors. First, the denser particle packing in lower slump concretes could lead to a more efficient arrangement, favouring the formation of near-spherical entrapped pores during compaction. On the other hand, the greater fluidity of workable concrete might allow for increased pore deformation, possibly leading to less spherical pore shapes. Second, the reduced workability of stiffer mixes may limit the deformation of rising bubbles during compaction, thereby maintaining their inherently spherical form. In contrast, bubbles within more fluid, workable concrete could have a higher potential to deviate from their original spherical shape, especially as they collide with aggregates under the forces of vibration. These interpretations, although plausible, require further research for verification.

Nonetheless, it is important to consider the potential drawbacks associated with non-spherical pores in concrete. Non-spherical or irregularly shaped pores can create stress concentrations [33] within concrete, as they lead to a lower load-carrying capacity [34] and increase the vulnerability to cracking [35]. Van den Heever [34] observed that concrete specimens exhibiting a drop in pore sphericity of approximately 19% showed lower compressive strengths compared to their counterparts with more spherical pores. This drop is attributed to the enhanced stress concentrations around irregularly shaped pores, compromising the structural integrity of the concrete. Therefore, it is important to minimize the presence of such pores within concrete by proper compaction, especially for more workable concretes.

3.3. Segregation analysis

To visualize the segregation within each sample, density profiles were formed by plotting the density of the sawn discs against each disc height, as shown in Fig. 8. Significant variations in density can be observed in the 20- and 45-second compacted specimens of the S3 and S4 groups, which denotes the occurrence of segregation. In these samples, the density increases considerably with height, indicating the presence of segregation due to the higher density of aggregates compared to the cement matrix. On the other hand, the S2 group exhibits minor fluctuations and the least variation in density across the specimen for the three vibration times of 5, 20, and 45 s. Similarly, the S3–5 and S4–5 samples show relatively consistent densities without major variations. It is worth noting that for S2–5, S3–5, and S4–5, the

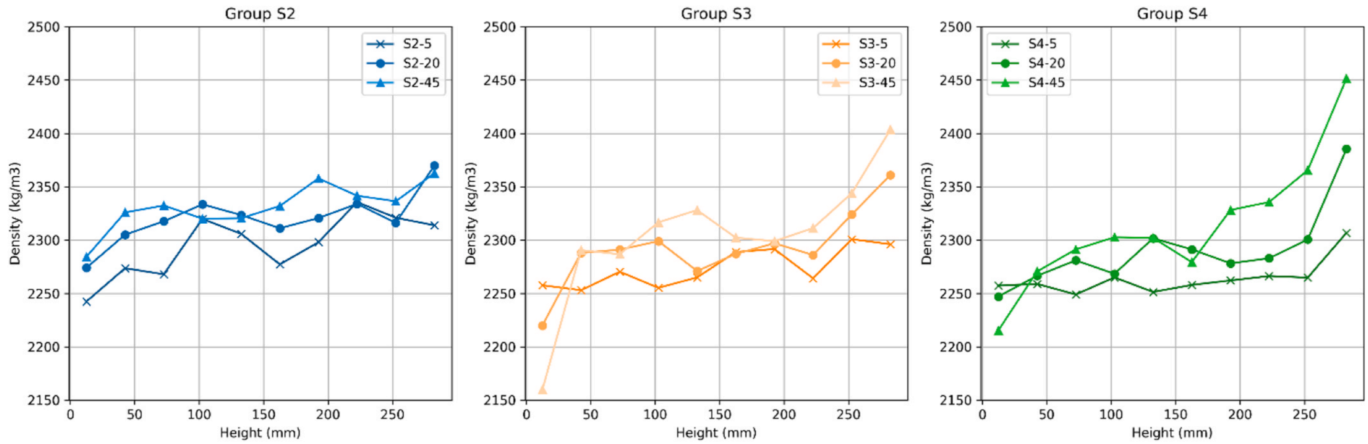

Fig. 8. Density variation along the height of concrete specimens for the three slump groups.

densities of the discs were on average much lower than their counterparts compacted for longer times, which is an indicator of the presence of extra entrapped pores due to insufficient compaction – as shown in Section 3.2.2.

The standard deviation and range of densities were calculated to assess the level of segregation within each sample, and the results are summarized in Table 7. Minor segregation is observed in the S2 group, as indicated by the standard deviation remaining below 30 kg/m^3 , a trend also seen in the S3–5 and S4–5 samples. In contrast, the remaining samples in the S3 and S4 groups exhibit higher levels of segregation, with the standard deviation of densities surpassing 30 kg/m^3 for both S3–20 and S4–20 and reaching nearly 60 kg/m^3 for both S3–45 and S4–45. The density variation follows a similar trend, with values ranging from 138 kg/m^3 to 244 kg/m^3 for S3–20, S3–45, S4–20, and S4–45, indicating significant segregation. Conversely, the density ranges for the remaining five specimens vary from 48 kg/m^3 to 96 kg/m^3 , less than half of that observed in their highly segregated counterparts.

Based on the previous observations, we can conclude that stiffer concretes (slump class of S2) are much harder to segregate, as both standard deviation and range of densities either remained similar or even decreased as the compaction time increased. On the other hand, for more workable concrete mixes, increasing the compaction time greatly affects the level of segregation. For instance, compacting S3–20 for 15 s longer than S3–5, resulted in almost double the standard deviation of densities and three times the range. Moreover, further increasing that time by 25 s doubled the values for both the standard deviation and range.

It is essential to examine the relationship between segregation and entrapped porosity across the height of the specimens. In the S3 and S4 groups, where the vibration time is 20 s or 45 s, we observed minimal entrapped pores distributed across the height of the four samples (see Fig. 3), However, these specimens exhibit a significant degree of segregation. Conversely, when the vibration time was limited to 5 s (S3–5 and S4–5), segregation was effectively minimized. However, at various locations, the entrapped porosity surpassed the 2% threshold. This observation suggests that while longer compaction times can help expel undesired entrapped pores, they can also contribute to segregation-related issues that should be considered during the compaction process. On the other hand, the S2 group exhibited minimal sensitivity to segregation with an increased compaction time, while effectively expelling more entrapped air. This finding implies that for stiffer concrete, longer compaction times can be safely employed to remove a greater amount of entrapped pores without a significant risk of segregation.

Table 7
Standard deviation and range of densities for the 10 discs of each sample.

Sample	Standard Deviation of Densities (kg/m^3)	Range of Densities (kg/m^3)
S2-5	28	93
S2-20	23	96
S2-45	21	78
S3-5	17	48
S3-20	34	141
S3-45	58	244
S4-5	15	58
S4-20	35	138
S4-45	60	236

3.4. General discussion

In this study, the authors conducted a comprehensive investigation of various characteristics of entrapped pores in hardened concrete using XCT. These characteristics encompassed the total amount of entrapped pores, the distribution of entrapped pores along the height of the specimens, the pore size distribution, and the sphericity of the pores. The findings revealed that while the total amount of entrapped pores may fall within acceptable limits, significant concentrations of entrapped pores were observed within the specimens, potentially giving rise to durability and strength issues. Moreover, particularly in cases of higher slumps, these accumulations of entrapped pores exhibited less spherical shapes, which can lead to heightened stress concentrations within the concrete.

Based on the findings of this study, we can suggest some practical advice to take into consideration for casting concretes with different consistencies. For low slump concrete such as S2, extended vibration significantly benefits the hardened concrete. While S2 initially retains notable entrapped porosity, especially in localized sections, its low tendency toward segregation makes longer vibration times advantageous. Prolonging the compaction time effectively expels entrapped air, thereby optimizing the strength and durability of the concrete. Consequently, employing extended vibration durations is recommended to enhance the properties of S2 concrete.

As the slump increases, expelling entrapped pores becomes more efficient, but pore sphericity diminishes, leading to stress concentrations, particularly where pores cluster. These clusters were more prevalent in S3 than in S4 concrete, though S4 pores were less spherical. The highest segregation sensitivity was noted in S4, demanding a balanced compaction approach. For S4, shorter vibration times, coupled with test specimen analysis, can prevent non-spherical pore accumulation and manage segregation risks. Meanwhile, S3, with lower segregation sensitivity, benefits from a moderately timed vibration, fine-tuned through specimen testing, to balance pore expulsion and sphericity without inducing pore clustering.

Having understood the characteristics of entrapped pores, this study emphasizes the necessity of future research to investigate the impact of entrapped porosity on both the mechanical and durability properties of concrete. Mechanical aspects such as compressive strength, flexural strength, and modulus of elasticity could be influenced by the total entrapped porosity and the concentration of entrapped pores within a specimen. Similarly, the distribution of pores, along with their shapes and sizes, could affect durability properties such as carbonation, freeze-thaw resistance, and chloride penetration. Furthermore, investigating the behaviour of entrapped pores in reinforced concrete is crucial, as the presence of reinforcement can influence the escape of pores during compaction. Additionally, examining the characteristics of entrapped pores in concretes compacted using a poker vibrator. This examination could offer differences between the behaviour of entrapped pores during the compaction by a table versus a poker vibrator. These avenues of research hold the potential to enhance our understanding of entrapped pores and their impact on concrete performance.

It should also be noted that there are some limitations to this study. The findings of this study are based on concretes cast with the same cement, aggregates, and chemical admixtures. To further generalize the findings, future research should consider including samples from concretes with varying types of cement, aggregates, and chemical admixtures. Furthermore, this study focuses on laboratory-scale experiments and core samples. While these provide valuable insights, the behaviour of entrapped pores and segregation in real-world construction scenarios may differ. In addition, the resolution of XCT scanning is always limited by the size of the sample. Although the sample used represented a significant part of the whole specimen, other methods could also be used to investigate larger size samples, such as digital image analysis. The use of other methods could also provide complementary insights and a more comprehensive understanding of the pore characteristics.

4. Conclusions

In the process of concrete compaction, despite efforts to remove entrapped air, a certain number of entrapped pores inevitably remain within the material. The presence and characteristics of these entrapped pores are influenced by factors such as concrete composition, placement, workability, and compaction time. This study employed XCT to thoroughly examine the characteristics of entrapped pores in compacted concrete samples. Through the casting of specimens with varying workability levels and subjecting them to different compaction durations, followed by XCT scanning, a comprehensive analysis of the entrapped porosity data was conducted. Based on the analysis of this data, we draw the following conclusions:

- As vibration duration increases, its interaction with concrete slump significantly influences entrapped porosity. A decrease in porosity by almost 40% is observed when the slump increases from S2 to S4, as the vibration time remains 5 s, indicating significant porosity expulsion with increased workability. However, this effect lessens with longer vibration times: a 20-second vibration yields only a 20% reduction, and at 45 s, slump differences cease to affect porosity levels. This pattern suggests that the impact of workability on porosity expulsion diminishes with extended vibration.
- High entrapped porosity regions can decrease in size up to 60% as the compaction time is increased for the same workability level. Similarly, for the same compaction time, increasing the workability of the concrete leads to a reduction of around 40% in the extent of these high porosity regions.
- While slump class S2 concrete shows stable segregation with increased vibration time, reducing entrapped porosity, S3 and S4 concretes exhibit heightened sensitivity. For S3, segregation doubles with a 28% porosity decrease from 5 to 20 s and increases 70% for another 28% reduction from 20 to 45 s. For S4, segregation more than doubles for an 8% porosity drop from 5 to 20 s, and doubles again with a 38% reduction from 20 to 45 s. This trend highlights the segregation sensitivity of more workable concretes during air expulsion.
- Areas of concentrated entrapped pores are identified within compacted concrete. This is highlighted by the presence of regions with high entrapped porosity within cores, where the entrapped air content could reach up to 5%. Notably, these regions can occur at various heights within the concrete specimen.
- The highest contribution to the total entrapped porosity comes from pores that fall within the volumetric range of 10–50 mm^3 (2.7–4.6 mm in diameter). The pores within that range represent around 25% of the total entrapped porosity, even though they comprise only about 3% of the number of entrapped pores.
- The sphericity of entrapped pores can vary greatly depending on the workability of concrete. For stiffer mixtures (S2), the pores are more likely to resemble perfect spheres, with around 44% of pores within the three S2 cores exhibiting a sphericity index of 0.9. In contrast, for more workable mixtures (S4), the pores show significantly less spherical shapes, with an average of only 5% of pores having a sphericity index of 0.9. The S3 mixtures, falling between the two extremes, demonstrate a moderate sphericity level, with approximately 21% of pores exhibiting a sphericity index of 0.9.
- The value and location of the maximum entrapped porosity varies from sample to sample and do not necessarily depend on the compaction time. As for the same workability, increasing the vibration time does not necessarily decrease the maximum entrapped porosity value. Furthermore, the location of the highest entrapped porosity varies greatly among the samples from 10 mm up to 225 mm from the surface.

In conclusion, this research highlights the crucial role of compaction time and concrete workability in dictating the characteristics of entrapped pores within hardened concrete. These factors significantly influence the distribution, size, and shape of the pores, which can impact the strength and durability of concrete. It is therefore essential to find the right balance: selecting a suitable workability and allowing enough vibration time to remove as many entrapped pores as possible, all while avoiding the risk of segregation.

CRediT authorship contribution statement

Punkki Jouni: Writing – review & editing, Supervision, Resources, Project administration, Funding acquisition, Conceptualization. **Kuva Jukka:** Writing – review & editing, Visualization, Software, Resources, Methodology, Investigation, Data curation. **Ahmed Hassan:** Writing – review & editing, Writing – original draft, Visualization, Validation, Methodology, Investigation, Formal analysis, Data curation, Conceptualization.

Declaration of Competing Interest

The authors declare that they have no known competing financial interests or personal relationships that could have appeared to influence the work reported in this paper.

Acknowledgement

This study was financially supported by the co-operation agreement with the Finnish Concrete Industry [project number 700721], and the x-ray tomography was supported by the Academy of Finland via RAMI infrastructure [project number 293109].

References

[1] S.Y. Chung, P. Sikora, T. Rucinska, D. Stephan, M. Abd Elrahman, Comparison of the pore size distributions of concretes with different air-entraining admixture dosages using 2D and 3D imaging approaches, Mater. Charact. 162 (2020), https://doi.org/10.1016/j.matchar.2020.110182.

[2] A. Koenig, Analysis of air voids in cementitious materials using micro X-ray computed tomography (μXCT), Constr. Build. Mater. 244 (2020), https://doi.org/10.1016/j.conbuildmat.2020.118313.
[3] A. du Plessis, W.P. Boshoff, A review of X-ray computed tomography of concrete and asphalt construction materials, Constr. Build. Mater. 199 (2019) 637–651, https://doi.org/10.1016/j.conbuildmat.2018.12.049.
[4] Y. Song, C. Shen, R.M. Damiani, D.A. Lange, Image-based Restoration of the Concrete Void System Using 2D-to-3D Unfolding Technique Evaluating Freeze-Thaw Durability of Railroad Concrete Crossties View project EllisDon View project, Constr. Build. Mater. 270 (2020), https://doi.org/10.20944/preprints202011.0259.v1.
[5] P.K. Mehta, P.J.M. Monteiro, Concrete microstructure, properties, and materials, 3rd ed., McGraw-Hill Professional Publishing, 2005.
[6] S. Guo, Q. Dai, X. Sun, Y. Sun, Z. Liu, Ultrasonic techniques for air void size distribution and property evaluation in both early-age and hardened concrete samples, Appl. Sci. (Switz.) 7 (2017) 1–18, https://doi.org/10.3390/APP7030290.
[7] C. Thomas, J. Setién, J.A. Polanco, J. de Brito, F. Fiol, Micro- and macro-porosity of dry- and saturated-state recycled aggregate concrete, J. Clean. Prod. 211 (2019) 932–940, https://doi.org/10.1016/j.jclepro.2018.11.243.
[8] Y. Chen, J. Kuva, A. Mohite, Z. Li, H. Rahier, F. Al-Neshawy, J. Shu, Investigation of the Internal Structure of Hardened 3D-Printed Concrete by X-CT Scanning and Its Influence on the Mechanical Performance, Materials 16 (2023), https://doi.org/10.3390/ma16062534.
[9] American Concrete Institute, Guide for Consolidation of Concrete, 2005.
[10] ASTM C457/C457M – 16. Standard Test Method for Microscopical Determination of Parameters of the Air-Void System in Hardened Concrete, (2016). https://doi.org/10.1520/C0457_C0457M-16.
[11] Suomen Betoniyhdistys ry, Betonin Laadunvarmistus. Osa 1-Betonin ilmahuokosparametrien määritys ohuthieistä, [Determination of concrete air pore parameters from thin sections] Suomen Betoniyhdistys ry, 2020. www.betoniyhdistys.fi. (In Finnish).
[12] American Concrete Institute, Report on behavior of fresh concrete during vibration, American Concrete Institute, 2008.
[13] A.M. Neville, Properties of concrete, 5th ed, Pearson, Harlow, 2011. https://aalto.finna.fi/Record/alli.555584.
[14] Cement Concrete & Aggregates Australia, Compaction of Concrete, 2006.
[15] SFS-EN 12350–7: 2019 Testing fresh concrete – Part 7: Air content., (2019).
[16] EN480–11 Determination of air void characteristics in hardened concrete, 2005.
[17] P.C. Fonseca, G.W. Scherer, An image analysis procedure to quantify the air void system of mortar and concrete, Mater. Struct. /Mater. Et. Constr. 48 (2015) 3087–3098, https://doi.org/10.1617/s11527-014-0381-9.
[18] T. Ojala, Y. Chen, J. Punkki, F. Al-Neshawy, Characteristics of entrained air voids in hardened concrete with the method of digital image analysis coupled with schwartz-saltykov conversion, Materials 14 (2021), https://doi.org/10.3390/ma14092439.
[19] B. Moravcová, P. Possl, P. Misák, M. Blažek, Possibilities of determining the air-pore content in cement composites using computed tomography and other methods, Mater. Tehnol. 50 (2016) 491–498, https://doi.org/10.17222/mit.2014.193.
[20] K.Y. Kim, T.S. Yun, J. Choo, D.H. Kang, H.S. Shin, Determination of air-void parameters of hardened cement-based materials using X-ray computed tomography, Constr. Build. Mater. 37 (2012) 93–101, https://doi.org/10.1016/j.conbuildmat.2012.07.012.
[21] H. Lu, K. Peterson, O. Chernoloz, Measurement of entrained air-void parameters in Portland cement concrete using micro X-ray computed tomography, Int. J. Pavement Eng. 19 (2018) 109–121, https://doi.org/10.1080/10298436.2016.1172705.
[22] J. Yuan, Y. Wu, J. Zhang, Characterization of air voids and frost resistance of concrete based on industrial computerized tomographical technology, Constr. Build. Mater. 168 (2018) 975–983, https://doi.org/10.1016/j.conbuildmat.2018.01.117.
[23] T.S. Yun, K.Y. Kim, J. Choo, D.H. Kang, Quantifying the distribution of paste-void spacing of hardened cement paste using X-ray computed tomography, Mater. Charact. 73 (2012) 137–143, https://doi.org/10.1016/j.matchar.2012.08.008.
[24] Á. Mena Alonso, D.C. González Cabrera, J. Mínguez Algarra, M.Á. Vicente Cabrera, La tomografía computerizada más allá de la medicina: Aplicaciones al estudio microestructural del hormigón y otros materiales de la ingeniería, Hormig. Y. Acero 71 (2020) 7–19, https://doi.org/10.33586/hya.2020.3020.
[25] M.A. Vicente, Á. Mena, J. Mínguez, D.C. González, Use of computed tomography scan technology to explore the porosity of concrete: Scientific possibilities and technological limitations, Appl. Sci. (Switz.) 11 (2021), https://doi.org/10.3390/app11188699.
[26] G.L. Balázs, É. Lublóy, T. Földes, Evaluation of Concrete Elements with X-Ray Computed Tomography, J. Mater. Civ. Eng. 30 (2018), https://doi.org/10.1061/(asce)mt.1943-5533.0002389.
[27] J.P. Moretti, A. Sales, V.A. Quarcioni, D.C.B. Silva, M.C.B. Oliveira, N.S. Pinto, L.W. S.L. Ramos, Pore size distribution of mortars produced with agroindustrial waste, J. Clean. Prod. 187 (2018) 473–484, https://doi.org/10.1016/j.jclepro.2018.03.219.
[28] S. Beucher, C. Lantuéjoul, Use of Watersheds in Contour Detection, 1979. 〈https://www.researchgate.net/publication/230837989〉.
[29] S. Popovics, A review of the concrete consolidation by vibration, Mater. Struct. /Mater. Et. Constr. 6 (1973).
[30] SFS-EN 12350–2: 2019 Testing fresh concrete – Part 2: Slump test, 2019.
[31] SFS-EN 12390–7: 2019 Testing hardened concrete – Part 7: Density of hardened concrete, 2019.
[32] I. Cruz-Matías, D. Ayala, D. Hiller, S. Gutsch, M. Zacharias, S. Estradé, F. Peiró, Sphericity and roundness computation for particles using the extreme vertices model, J. Comput. Sci. 30 (2019) 28–40, https://doi.org/10.1016/j.jocs.2018.11.005.
[33] T. Davis, D. Healy, A. Bubeck, R. Walker, Stress concentrations around voids in three dimensions: The roots of failure, J. Struct. Geol. 102 (2017) 193–207, https://doi.org/10.1016/j.jsg.2017.07.013.
[34] M. van den Heever, A. du Plessis, J. Kruger, G. van Zijl, Evaluating the effects of porosity on the mechanical properties of extrusion-based 3D printed concrete, Cem. Concr. Res. 153 (2022), https://doi.org/10.1016/j.cemconres.2021.106695.
[35] J. Li, S. Cao, W. Song, Distribution development of pore/crack expansion and particle structure of cemented solid-waste composites based on CT and 3D reconstruction techniques, Constr. Build. Mater. 376 (2023) 130966, https://doi.org/10.1016/j.conbuildmat.2023.130966.